

Möbius Kondo Insulators

Po-Yao Chang,^{1,*} Onur Erten,^{1,2} and Piers Coleman^{1,3,†}

¹*Center for Materials Theory, Rutgers University,
Piscataway, New Jersey, 08854, USA*

²*Max Planck Institute for the Physics of Complex Systems, Dresden, 01187, Germany*

³*Department of Physics, Royal Holloway,
University of London, Egham, Surrey TW20 0EX, UK*

Abstract

Heavy fermion materials have recently attracted attention for their potential to combine topological protection with strongly correlated electron physics. To date, the ideas of topological protection have been restricted to the heavy fermion or “Kondo” insulators with the simplest point-group symmetries. Here we argue that the presence of nonsymmorphic crystal symmetries in many heavy fermion materials opens up a new family of topologically protected heavy electron systems. Re-examination of archival resistivity measurements in nonsymmorphic heavy fermion insulators $\text{Ce}_3\text{Bi}_4\text{Pt}_3$ and CeNiSn reveals the presence of low temperature conductivity plateau, making them candidate members of the new class of material. We illustrate our ideas with a specific model for CeNiSn , showing how glide symmetries generate surface states with a novel Möbius braiding that can be detected by ARPES or non-local conductivity measurements. One of the interesting effects of strong correlation, is the development of partially localization or “Kondo breakdown” on the surfaces, which transforms Möbius surface states into quasi-one dimensional conductors, with the potential for novel electronic phase transitions.

* pychang@physics.rutgers.edu

† coleman@physics.rutgers.edu

The discovery of topological phases of matter, initiated by the pioneering works on quantum Hall states in 1980s[1–3] has now evolved into the broad notion of symmetry-protected topological states of matter. Heavy fermion or “Kondo” insulators have recently emerged as a particularly promising platform to study the interplay between topological phases and strong electron interactions[4, 5]. In topological Kondo insulators (TKIs), the strong interaction between conduction electrons and local magnetic moments leads to the formation of a narrow gap associated with the development of Kondo singlets which screen the local moments[6–9]. In SmB_6 , the oldest known Kondo insulator, the existence of metallic surface states has been demonstrated by transport experiments[10–13] and angle-resolved photoemission spectroscopy (ARPES)[14–16]. These results have identified SmB_6 as a promising candidate for a TKI.

One of the important aspects of these materials is the interplay between crystalline symmetry and topological order. To date, the main focus of interest in heavy fermion materials has been limited to the simplest crystalline symmetries. In this work, we expand this notion to a wider class of heavy fermion materials in which unique topological features can arise from the combination of fractional translations and by point group transformations known as nonsymmorphic symmetries. Examples of Kondo insulators with non-symmorphic symmetries include $\text{Ce}_3\text{Bi}_4\text{Pt}_3$ [4, 17], and CeNiSn , CeRhSb , CeIrSb [19–21]. The observation of resistivity saturation at low temperatures in $\text{Ce}_3\text{Bi}_4\text{Pt}_3$ under pressure[4] and CeNiSn [22] with Sb doping, closely resemble the conductivity plateau of topological SmB_6 , strongly suggesting that these nonsymmorphic Kondo insulators are topologically nontrivial.

To illustrate the topological effects of nonsymmorphic symmetries in heavy fermion systems, here we study CeNiSn as a representative member of this new new class of TKIs. A central element of our theory is a tight-binding model of CeNiSn with all its salient symmetries. The structure of CeNiSn belongs to nonsymmorphic space group No. 62 ($Pnma$), containing three glide reflections, three screw rotations and inversion symmetry, as shown in Fig. 1. Glide reflections and screw rotations are nonsymmorphic symmetries, which combine a point group operation (mirror or rotation) and a fractional lattice translation. We find that these symmetries permit nonsymmorphic Kondo insulators to develop a protected surface state, composed of two Dirac cones. Unlike regular topological insulators, in which scattering between two surface Dirac cones can open a gap without breaking time-reversal symmetry, the autonomy of these surface states is stabilized by glide reflection and time-reversal symmetry [1, 24]. Moreover, nonsymmorphic symmetries give rise to a momentum dependent twist that enables the surface states to be detached from the bulk

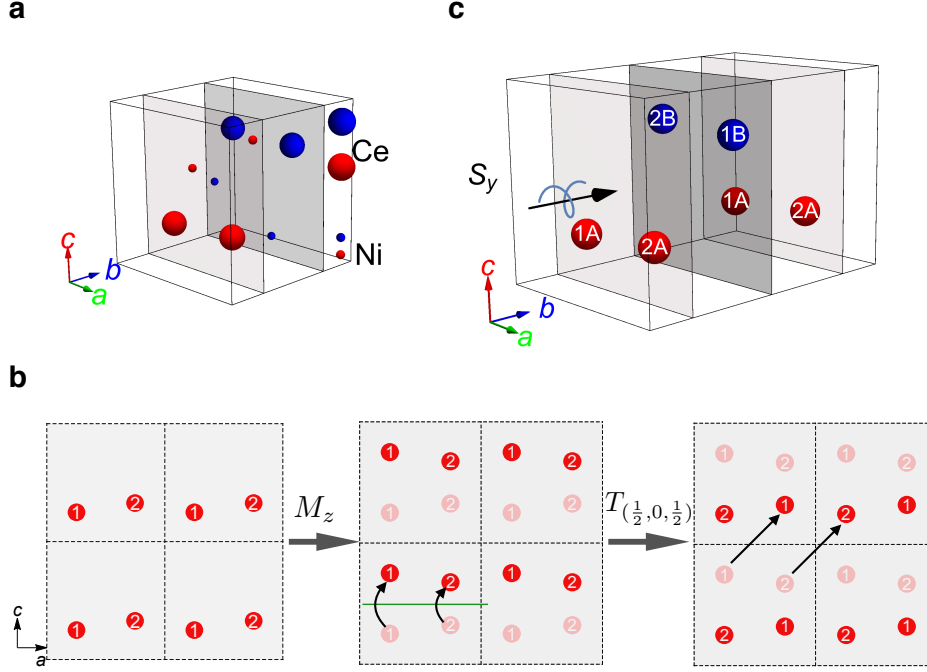


FIG. 1. **Crystal structure of CeNiSn:** showing **a** the location of the Ce and Ni atoms, denoted by red and blue spheres. There are four equivalent Ce sites $\{1A, 2A, 1B, 2B\}$ related by glide reflections and screw rotations. The Ce and Ni atoms form zigzag chains which reside on two planes labeled *A* (light gray) and *B* (dark gray), stacked along the *b*-axis. **b**, showing the glide reflection $G_z = T_{(1/2,0,1/2)} M_z$ which connects the Ce sites on different chains $G_z : (1A, 2A, 1B, 2B) \rightarrow (2A, 1A, 2B, 1B)$. **c** showing the screw rotation $S_y = T_{(0,1/2,0)} R_y^\pi$ which connects the chains in different planes $S_y : (1A, 2A, 1B, 2B) \rightarrow (1B, 2B, 1A, 2A)$.

on the glide plane. Following recent studies[1, 24–27], we refer to these states as Möbius-twisted surface states. From the bulk-boundary correspondence, we are able to define a \mathbb{Z}_4 topological invariant, and discuss the experimental signatures of such a phase. One of the important effects that sets these topological insulators apart from their weakly interacting counterparts, is the possibility of breakdown of the Kondo effect at the surface[28]. We find that this breakdown has a particularly dramatic effect on the Möbius-twisted surface states, giving rise to quasi-one dimensional Fermi surfaces.

I. TIGHT-BINDING HAMILTONIAN AND NONSYMMORPHIC SYMMETRIES

We begin by constructing a tight-binding Hamiltonian for CeNiSn. CeNiSn has an orthorhombic ϵ -TiNiSi structure belonging to nonsymmorphic space group No. 62, $Pnma$, which contains an inversion P , a screw rotation $S_y = T_{(0,1/2,0)}R_y^\pi$, and a glide reflection $G_z = T_{(1/2,0,1/2)}M_z$, where R_i^π denotes a π rotation about the i -axis, M_j refers to the mirror operation in the plane perpendicular to the j -axis, and $T_{(a,b,c)}$ is the translation operator along $a\hat{x} + b\hat{y} + c\hat{z}$. There are four equivalent Ce sites in the unit cell which we label as $\{1A, 2A, 1B, 2B\}$ as shown in Fig 1. The Cerium sites form zig-zag chains in the ac plane which are stacked along the c direction. Fig. 1b shows how glide reflection connects inter-chain sites $G_z : (1A, 2A, 1B, 2B) \rightarrow (2A, 1A, 2B, 1B)$. These layers are then arranged in an alternating fashion along the b direction; the alternating layers are related by the screw rotation $S_y : (1A, 2A, 1B, 2B) \rightarrow (1B, 2B, 1A, 2A)$ as shown in Fig. 1c. In the following discussion, we re-scale the dimensions a , b and c of the unit cell to be unity. When applying the glide reflection and the screw rotation symmetries twice, the system is shifted by a lattice translation, but the process also involves a double reflection or π rotation. The half-integer character of the electrons means that reflections or π -rotations square to -1 , and this additional factor means appears in the square of glide reflection and screw rotations as follows:

$$\begin{aligned} G_z^2 &= T_{(1/2,0,1/2)}M_zT_{(1/2,0,1/2)}M_z \\ &= T_{(1,0,0)}M_z^2 = -T_{(1,0,0)} \equiv -e^{-ik_x}. \end{aligned} \quad (1)$$

$$\begin{aligned} S_y^2 &= T_{(0,1/2,0)}R_y^\pi T_{(0,1/2,0)}R_y^\pi \\ &= T_{(0,1,0)}[R_y^\pi]^2 = -T_{(0,1,0)} \equiv -e^{-ik_y}. \end{aligned} \quad (2)$$

Band structure calculations[29–31] indicate that the relevant orbitals near the chemical potential derive from the Ce $4f$ -electrons and Ni $3d$ -electrons. We now construct a simplified model involving these two sets of orbitals. A key ingredient of our model is the hybridization between the f and d states which involves the transfer of one unit of angular momentum from spin, to orbital angular momentum. As a result, the hybridization develops a p-wave form-factor[28], and can be modelled by a simpler model of spin-orbit p orbitals hybridizing with s -wave conduction electrons. We project the Wannier states of these two sets of orbitals onto the common sites of the

Cerium atoms. The resulting tight-binding Hamiltonian has the structure

$$\mathcal{H}(\mathbf{k}) = \begin{pmatrix} \mathcal{H}^c(\mathbf{k}) & V(\mathbf{k}) \\ V^\dagger(\mathbf{k}) & \mathcal{H}^f(\mathbf{k}) \end{pmatrix}, \quad (3)$$

where $V(\mathbf{k})$ is the hybridization matrix, \mathcal{H}^c and \mathcal{H}^f are the nearest hopping matrices for the conduction and f -electrons respectively. The detailed structure of this Hamiltonian, which respects the full nonsymmorphic symmetries of the lattice, is provided in the methods.

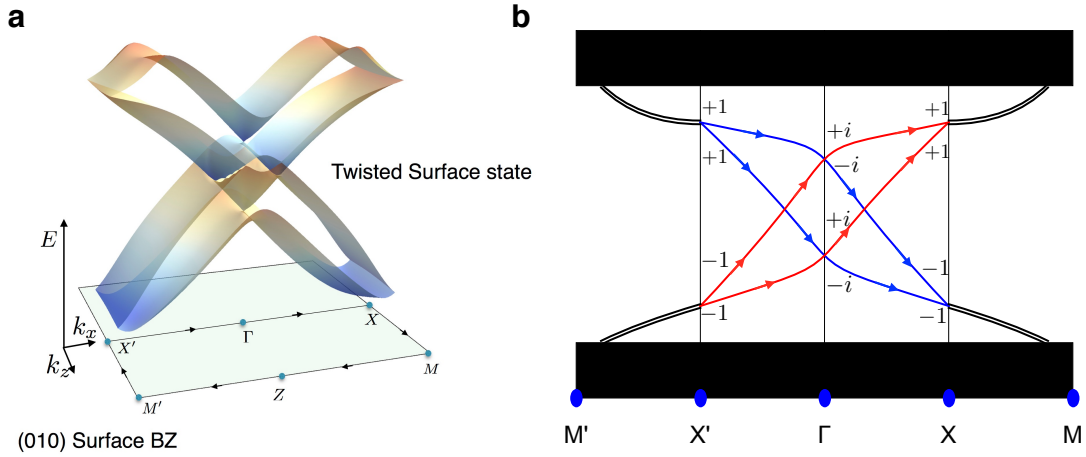


FIG. 2. A pair of Möbius twisted surface states on the (010) surface. **a.** Three dimensional plot of the dispersion on the (010) surface. The two Möbius twisted surface states are detached from the bulk along the glide line ($X'\Gamma X$). **b.** Schematic showing dispersion along the glide line $X'\Gamma X$, where red and blue lines correspond to states with positive and negative glide eigenvalues g_{\pm} , respectively. Along XM ($X'M'$) the surface states are doubly degenerate due to a combination of time-reversal and glide symmetry, $\mathcal{T}\mathcal{G}_z$. The imaginary glide eigenvalues $\pm i$ at the Γ point force the members of each Kramers pair to belong to different glide sectors, but at the X (X') points the real glide eigenvalues ± 1 mean that the members of a Kramers pair are in the same glide sector. The connectivity between Kramers pairs at the Γ and X (X') points gives rise to the Möbius character, for if one starts at X' and follows the red loop to X , one has to pass a second time around the loop on the blue line, before one returns to the origin.

II. TOPOLOGICAL SURFACE STATES WITH A MÖBIUS TWIST

One symmetry-preserving surface which respects to the glide reflection \mathcal{G}_z is the (010) surface. This surface is perpendicular to the glide plane (xy plane) and is also invariant under lattice trans-

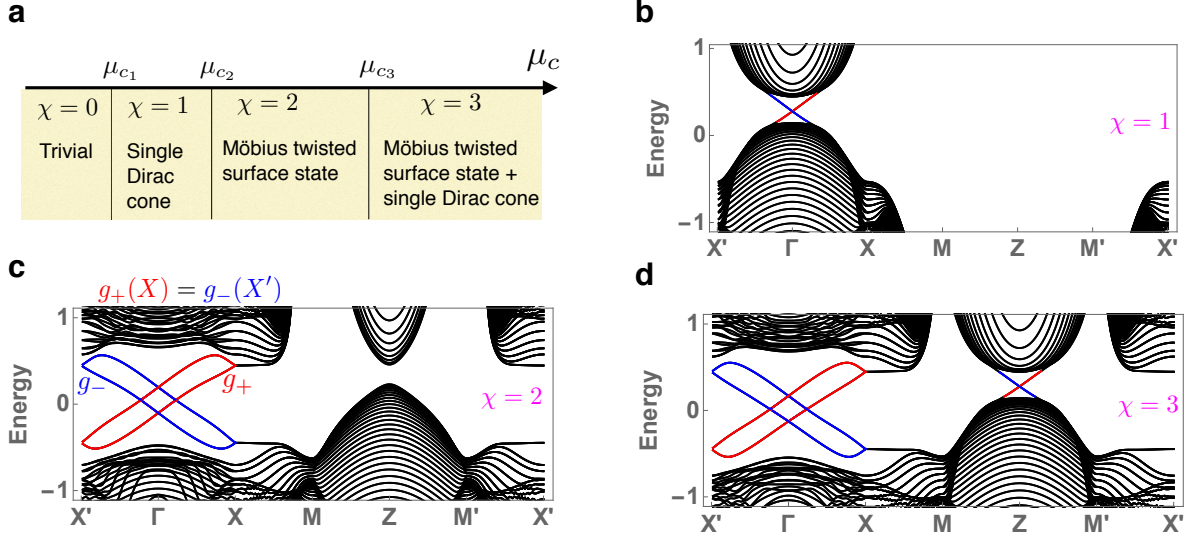


FIG. 3. \mathbb{Z}_4 topological invariants and the corresponding surface states: **a**, Four phases as the function of the chemical potential of conduction electrons μ_c , with $(\mu_{c_1}, \mu_{c_2}, \mu_{c_3}) = (-73, -60.5, -33)$ and the parameters used in equation (4) are $(\alpha, \beta, \gamma, a, b) = (0.525, 0.525, 0.1, 0.5, 0.5)$, $(t_x^e, t_y^e, t_z^e) = (5, -25, -10) = -20(t_x^f, t_y^f, t_z^f)$, and $\mu_c = -20\mu_f$. **b-d**, The energy spectra are computed in a (010) slab geometry for $\chi = 1, 2, 3$, respectively. Red and blue lines are the energy dispersion of surface states with positive and negative glide eigenvalues g_{\pm} , respectively. A Möbius twisted surface is located at the glide plane ($X'\Gamma X$) shown in **c** and **d**. This Möbius twisted surface is composed by two Dirac cones. Due to Kramers pairs at X point have the same glide eigenvalue and $g_+(X) = g_-(X')$, this Möbius twisted surface is detached from the bulk at the glide plane.

lations parallel to the surface. The surface energy dispersion as a function of (k_x, k_z) is computed by diagonalizing the Hamiltonian in a (010) slab geometry. The corresponding surface Brillouin zone (BZ) is shown in Fig. 2a. The glide lines on the surface BZ are the set of glide reflection invariant momenta, which are at $k_z = 0$ (path $X'\Gamma X$) and $k_z = \pi$ (path $M'ZM$). Along these lines, the Hamiltonian from equation (4) commutes with \mathcal{G}_z and can be block diagonalized into two sectors with two eigenvalues for \mathcal{G}_z , $g_{\pm}(k_x) = \pm ie^{-ik_x/2}$ along the glide lines.

On the glide lines along $X'\Gamma X$ or $M'ZM$, a pair of surface Dirac cones is stabilized by the glide reflection and time-reversal symmetry. To demonstrate this state (see Fig. 2b), we focus on path $X'\Gamma X$. At the $X(X')$ point, the glide eigenvalues are real (± 1), which implies that the members of each Kramers pair derive from the same glide sector, i.e., the glide eigenvalues for two Kramers pairs are $(+1, +1)$ and $(-1, -1)$. By contrast, at the Γ point, the glide eigenvalues

are imaginary ($\pm i$), so time reversal inverts the glide eigenvalue, which indicates that the members of each Kramers pair come from opposite glide sectors, i.e., the glide eigenvalues for two Kramers pairs are both $(+i, -i)$. When we connect two Kramers pairs at Γ point to two Kramers pairs at $X(X')$ point we obtain the hourglass structure of this surface state[24], which contains two Dirac cones at the Γ point (Fig. 2b). This surface state contains a Möbius twist, for if we follow the arrow from Fig. 2b along the loop $X'\Gamma X$, we need go around the loop twice: once on a red and once on a blue branch, before returning to the origin. Due to this unusual connectivity, the surface state can be detached from the bulk along the loop $X'\Gamma X$. Fig. 2a displays the result of a band-calculation on a strip, showing the Möbius-twisted character.

The presence or absence of a Möbius-twisted surface state on the (010) surface defines a \mathbb{Z}_2 variable. When we combine this with the additional \mathbb{Z}_2 variable associated with the possibility of forming a strong topological insulator, by introducing an additional odd number of Dirac cones on every surface, we see that the combination of time-reversal and non-symmorphic symmetries gives rise to a \mathbb{Z}_4 topological invariant χ , for which we can construct a corresponding \mathbb{Z}_4 index (see Supplementary Information and also Ref. [1]), as shown in Fig. 3a. $\chi = 0$ corresponds to a trivial insulator with no gapless surface states. $\chi = 1$ corresponds to a strong topological insulating phase with one single surface Dirac cone (Fig. 3b). $\chi = 2$ corresponds to a nonsymmorphic topological insulator with a Möbius twisted surface state along $X'\Gamma X$ ($M'ZM$) path (Fig. 3c), while $\chi = 3$ corresponds to a strong topological insulating phase with three surface Dirac cones (Fig. 3d).

In our model calculations, we also observe a double Dirac cone like surface state on (001) surface, where the crossings are located at $(k_x, k_y) = (\pm k_0, 0)$. However at the mirror plane $k_y = 0$, this surface state is gapped and is not protected by mirror symmetry \mathcal{M}_y and time-reversal symmetry \mathcal{T} , so this state will likely be absent in the real material.

III. DISCUSSION

We have shown that CeNiSn and Kondo insulators with nonsymmorphic symmetries have the potential to form a new class of topological Kondo insulators with unusual surface states. CeNiSn is of course a low-carrier density metal, with a small Fermi surface derived from an indirect band-gap closure or a lightly doped conduction band[32, 33], but such small bulk Fermi surfaces are readily localized by disorder or substitution. This is the likely explanation of the observation of a resistivity plateau below 10K in antimony-doped CeNiSn_{1-x}Sb_x[22], where the observation of a

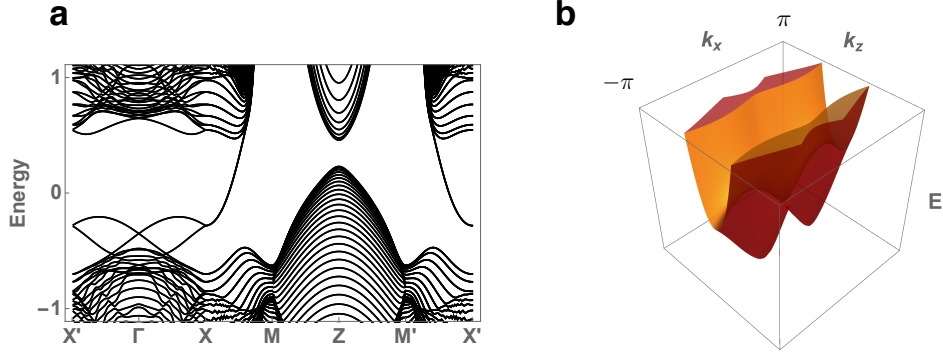


FIG. 4. **a**, Showing the effect of Kondo breakdown on the dispersion of the Möbius-twisted surface state, causing the Dirac points to sink into the valence band. **b**, Three dimensional plot showing the quasi-one dimensional dispersion of Möbius-twisted surface state in the presence of Kondo breakdown.

resistivity plateau most likely derives from a metallic topological surface states, as in the case of SmB_6 . Moreover the V-shape density of states deduced from NMR experiments and point-contact spectroscopy[34–36] can be accounted for as a signatures of Dirac cone surface states. The large magnetoresistance for fields perpendicular to the a axis[32] may be a consequence of metallic surface in the (010) plane, combined with an insulating surface on the (100) and (001) planes. Although the above discussion has focussed on CeNiSn , we note that the nonsymmorphic Kondo insulator $\text{Ce}_3\text{Bi}_4\text{Pt}_3$ also displays a resistivity plateau. Remarkably, in the presence of pressure, the resistivity plateau persists up to 100K[4] [See supplementary material]. These early experimental results provide strong circumstantial support for the topological nature of these nonsymmorphic Kondo insulators and provide a strong motivation for further detailed investigation.

The confirmation of these ideas requires a direct probe of Möbius conducting surface states, either by ARPES measurements, or by non-local[10] or sample thickness dependent transport measurements[37]. One of the interesting challenges is to delineate Möbius surface states from single Dirac surface states. According to Ref. [38], one-dimensional chiral edge modes from ferromagnetic domain walls on the surface of SmB_6 have been observed with quantized e^2/h conductance. If an analogous ferromagnetic order emerges on a nonsymmorphic surface (induced by field or magnetic impurities), any Möbius state present will become gapped. The Landau levels of a Möbius surface state will contribute to quantized conductance $2(n + 1/2)e^2/h$, where n depends on the surface chemical potential. When the Fermi energy is in the gap, the conductance

only comes from the lowest Landau level with $n = 0$. The transport measurement presumably comes from both top and bottom surface that give rise to the total conductance $2e^2/h$, twice that observed in SmB_6 . Another way to detect twisted surface states is from Hall bar measurements. In contrast with the usual topological insulators, where the quantum Hall conductivity σ_H switches from $-e^2/h$ to e^2/h on gating, the twisted surface state will generate three values of quantized Hall conductivity. When the gate voltage is below(above) two cones, we have $\sigma_H = -e^2/h(e^2/h)$. Whereas the gate voltage is in between two cones, the Hall conductance will vanish, $\sigma_H = 0$.

The strong electron correlations in Kondo insulators opens up the possibility of many interesting phenomena, absent in their weakly interacting counterparts. Here, a particularly important phenomenon is the possibility of a surface breakdown of the Kondo effect[28]. Surface Kondo breakdown is based on the observation that the reduced coordination of the rare earth ions at the surface causes a reduction of in the surface Kondo temperature. In principle, competing instabilities such as magnetism can now be activated on the surface. The breakdown of the the Kondo singlets at the surface liberates a large number of conduction electrons which then dope the topological surface states. We have examined the effects of surface Kondo breakdown in Möbius surface states by recomputing the surface spectrum in the absence of the surface f-states. These calculations show that the Kondo breakdown causes the Dirac points in Möbius surface states to sink into the valence band as shown in Fig. 4a which then generates large Fermi surfaces [see Fig. 4b]. The detached nature of the Möbius surface state causes the resulting Fermi surfaces to become quasi one-dimensional along k_x direction. The interaction of the partially unscreened surface local moments with these quasi one-dimensional Fermi surfaces is expected to lead to a wide variety of surface electronic instabilities, including unconventional superconductivity[39] and charge or spin density wave instabilities.

Another interesting future direction is the possibility of nonsymmorphic topological superconductors. Promising candidates are UCoGe and URhGe , which share the same space group as CeNiSn [40, 41]. These materials exhibit spin-triplet superconductivity in coexistence with ferromagnetism. The topological classification of such superconductors is an intriguing future prospect.

IV. METHODS

In the momentum space, the tight-binding Hamiltonian is $H = \sum_{\mathbf{k}} \Psi(\mathbf{k})^\dagger \mathcal{H}(\mathbf{k}) \Psi(\mathbf{k})$, where $\Psi(\mathbf{k})$ is a sixteen component spinor, $\Psi(\mathbf{k}) = (\Psi_c(\mathbf{k}), \Psi_f(\mathbf{k}))^T$ with

$$\begin{aligned} \Psi_c(\mathbf{k}) &= (c_{1A\uparrow}(\mathbf{k}), c_{1A\downarrow}(\mathbf{k}), c_{2A\uparrow}(\mathbf{k}), c_{2A\downarrow}(\mathbf{k}), \\ &\quad c_{1B\uparrow}(\mathbf{k}), c_{1B\downarrow}(\mathbf{k}), c_{2B\uparrow}(\mathbf{k}), c_{2B\downarrow}(\mathbf{k})), \\ \Psi_f(\mathbf{k}) &= (f_{1A\uparrow}(\mathbf{k}), f_{1A\downarrow}(\mathbf{k}), f_{2A\uparrow}(\mathbf{k}), f_{2A\downarrow}(\mathbf{k}), \\ &\quad f_{1B\uparrow}(\mathbf{k}), f_{1B\downarrow}(\mathbf{k}), f_{2B\uparrow}(\mathbf{k}), f_{2B\downarrow}(\mathbf{k})), \end{aligned}$$

and

$$\mathcal{H}(\mathbf{k}) = \begin{pmatrix} \mathcal{H}^c(\mathbf{k}) & V(\mathbf{k}) \\ V^\dagger(\mathbf{k}) & \mathcal{H}^f(\mathbf{k}) \end{pmatrix}, \quad (4)$$

where $V(\mathbf{k})$ is the hybridization matrix, \mathcal{H}^c and \mathcal{H}^f are the nearest hopping matrices for conduction and f -electrons, respectively. In order to simplify our calculation, we introduce four sets of Pauli matrices: $\{\sigma_i\}$ acts on the spin basis; $\{\lambda_i\}$ acts on the basis of conduction electrons and f -electrons; $\{\tau_i\}$ acts on the basis of the atom labels 1 and 2; $\{\rho_i\}$ acts on the basis of the layer labels A and B .

From equation (4), the hybridization matrix has the form

$$V(\mathbf{k}) = \begin{pmatrix} V_A(\mathbf{k}) & V_{AB}(\mathbf{k}) \\ V_{BA}(\mathbf{k}) & V_B(\mathbf{k}) \end{pmatrix},$$

where

$$\begin{aligned} V_A(\mathbf{k}) &= \begin{pmatrix} 2it_2 \sin k_z & t_1 + \sigma_3 t_1 \sigma_3 e^{-ik_x} \\ -t_1 - \sigma_3 t_1 \sigma_3 e^{ik_x} & 2it_2 \sin k_z \end{pmatrix} = -V_B(-\mathbf{k}), \\ V_{AB}(\mathbf{k}) &= \begin{pmatrix} & t_3 - \sigma_2 t_3 \sigma_2 e^{-ik_y} \\ t_4 - \sigma_2 t_4 \sigma_2 e^{-ik_y} & \end{pmatrix}, \\ V_{BA}(\mathbf{k}) &= \begin{pmatrix} & \sigma_2 t_3 \sigma_2 e^{ik_y} - t_3 \\ \sigma_2 t_4 \sigma_2 e^{ik_y} - t_4 & \end{pmatrix}, \end{aligned}$$

with $t_1 = i(\alpha\sigma_1 + \beta\sigma_3)$, $t_2 = i\gamma\sigma_3$, $t_3 = i(a\sigma_2 + b\sigma_3)$, and $t_4 = i(a\sigma_2 - b\sigma_3)$.

The nearest hopping matrices for conduction electrons and f -electrons are

$$\begin{aligned} \mathcal{H}^l(\mathbf{k}) = & (2t_z^l \cos k_z - \mu^l) + 2t_x^l \cos \frac{k_x}{2} \left(\cos \frac{k_x}{2} \tau_1 + \sin \frac{k_x}{2} \tau_2 \rho_3 \right) \\ & + 2t_y^l \cos \frac{k_y}{2} \left(\cos \frac{k_y}{2} \tau_1 \rho_1 + \sin \frac{k_y}{2} \tau_1 \rho_2 \right), \end{aligned}$$

where $l = c, f$, t_i^l are the hopping amplitudes along i -direction, and μ^l are the bare energies of the isolated conduction electrons and f -electrons. In the Supplementary Information we perform the construction of this tight-binding Hamiltonian in detail.

We write down the matrix representations of symmetries as follows:

1. Time-reversal symmetry, $\mathcal{T}^{-1} \mathcal{H}(\mathbf{k}) \mathcal{T} = \mathcal{H}(-\mathbf{k})$, where $\mathcal{T} = i\sigma_2 \mathcal{K}$ with \mathcal{K} being the complex conjugation operator.
2. Inversion symmetry, $\mathcal{P}^{-1} \mathcal{H}(\mathbf{k}) \mathcal{P} = \mathcal{H}(-\mathbf{k})$, where $\mathcal{P} = \lambda_3 \rho_1$.
3. Glide reflection symmetry \mathcal{G}_z , $\mathcal{G}_z^{-1} \mathcal{H}(k_x, k_y, k_z) \mathcal{G}_z = \mathcal{H}(k_x, k_y, -k_z)$, where

$$\mathcal{G}_z(\mathbf{k}) = -ie^{-i\frac{k_x}{2}} \sigma_3 \left(\cos \frac{k_x}{2} \tau_1 + \sin \frac{k_x}{2} \tau_2 \rho_3 \right) \lambda_3.$$

4. Screw rotation symmetry \mathcal{S}_y , $\mathcal{S}_y^{-1} \mathcal{H}(k_x, k_y, k_z) \mathcal{S}_y = \mathcal{H}(-k_x, k_y, -k_z)$, where

$$\mathcal{S}_y(\mathbf{k}) = -ie^{-i\frac{k_y}{2}} \sigma_2 \left(\cos \frac{k_y}{2} \rho_1 + \sin \frac{k_y}{2} \rho_2 \right).$$

5. Mirror symmetry $\mathcal{M}_y = \mathcal{S}_y \mathcal{P}$, $\mathcal{M}_y^{-1} \mathcal{H}(k_x, k_y, k_z) \mathcal{M}_y = \mathcal{H}(k_x, -k_y, k_z)$, where

$$\mathcal{M}_y(\mathbf{k}) = -ie^{-i\frac{k_y}{2}} \sigma_2 \left(\cos \frac{k_y}{2} \rho_0 - i \sin \frac{k_y}{2} \rho_3 \right) \lambda_3.$$

In the spin-orbit coupled systems, reflection and π rotation square to -1 . We have $\mathcal{G}_z(\mathbf{k})^2 = -e^{-ik_x}$, $\mathcal{S}_y(\mathbf{k})^2 = -e^{-ik_y}$, and $\mathcal{M}_y(k_y = 0, \pi)^2 = -1$.

V. ACKNOWLEDGMENTS

The authors would like to thank Silke Paschen and Tyrel McQueen for discussions about CeNiSn. This work was supported by the Rutgers Center for Materials Theory group postdoc grant (Po-Yao Chang), US National Science Foundation grant grant DMR-1309929 (Onur Erten) and US Department of Energy grant DE-FG02-99ER45790 (Piers Coleman).

VI. AUTHOR CONTRIBUTIONS

All authors performed the calculations, discussed the results and prepared the manuscript.

VII. COMPETING FINANCIAL INTERESTS

The authors declare no competing financial interests.

-
- [1] Laughlin, R. B. Quantized Hall conductivity in two dimensions. Phys. Rev. B **23**, 5632–5633 (1981). URL <http://link.aps.org/doi/10.1103/PhysRevB.23.5632>.
- [2] Thouless, D. J., Kohmoto, M., Nightingale, M. P. & den Nijs, M. Quantized Hall Conductance in a Two-Dimensional Periodic Potential. Phys. Rev. Lett. **49**, 405–408 (1982). URL <http://link.aps.org/doi/10.1103/PhysRevLett.49.405>.
- [3] Haldane, F. D. M. Model for a Quantum Hall Effect without Landau Levels: Condensed-Matter Realization of the "Parity Anomaly". Phys. Rev. Lett. **61**, 2015–2018 (1988). URL <http://link.aps.org/doi/10.1103/PhysRevLett.61.2015>.
- [4] Dzero, M., Sun, K., Galitski, V. & Coleman, P. Topological Kondo Insulators. Phys. Rev. Lett. **104**, 106408 (2010). URL <http://link.aps.org/doi/10.1103/PhysRevLett.104.106408>.
- [5] Dzero, M., Sun, K., Coleman, P. & Galitski, V. Theory of topological Kondo insulators. Phys. Rev. B **85**, 045130 (2012). URL <http://link.aps.org/doi/10.1103/PhysRevB.85.045130>.
- [6] G. Aeppli, Z. F. Kondo insulators. Comm. Condens. Matter Phys. **15**, 155 (1992).
- [7] Fisk, Z. et al. Kondo insulators. Physica B: Condensed Matter **206-207**, 798 – 803 (1995). URL <http://www.sciencedirect.com/science/article/pii/092145269400588M>. Proceedings of the International Conference on Strongly Correlated Electron Systems.
- [8] Tsunetsugu, H., Sigrist, M. & Ueda, K. The ground-state phase diagram of the one-dimensional Kondo lattice model. Rev. Mod. Phys. **69**, 809–864 (1997). URL <http://link.aps.org/doi/10.1103/RevModPhys.69.809>.
- [9] Riseborough, P. S. Heavy fermion semiconductors. Adv. Phys. **49**, 257–320 (2000). URL <http://dx.doi.org/10.1080/000187300243345>.

- [10] Wolgast, S. *et al.* Low-temperature surface conduction in the Kondo insulator SmB_6 . Phys. Rev. B **88**, 180405 (2013). URL <http://link.aps.org/doi/10.1103/PhysRevB.88.180405>.
- [11] Kim, D. J. *et al.* Surface Hall Effect and Nonlocal Transport in SmB_6 : Evidence for Surface Conduction. Sci. Rep. **3**, 3150 (2013). URL <http://www.ncbi.nlm.nih.gov/pmc/articles/PMC3818682/>.
- [12] Kim, D. J., Xia, J. & Fisk, Z. Topological surface state in the Kondo insulator samarium hexaboride. Nat. Mater. **13**, 466–470 (2014). URL <http://dx.doi.org/10.1038/nmat3913>.
- [13] Thomas, S. *et al.* Weak Antilocalization and Linear Magnetoresistance in The Surface State of SmB_6 . ArXiv e-prints (2013). 1307.4133.
- [14] Neupane, M. *et al.* Surface electronic structure of the topological Kondo-insulator candidate correlated electron system SmB_6 . Nat. Commun. **4** (2013). URL <http://dx.doi.org/10.1038/ncomms3991>.
- [15] Xu, N. *et al.* Surface and bulk electronic structure of the strongly correlated system SmB_6 and implications for a topological Kondo insulator. Phys. Rev. B **88**, 121102 (2013). URL <http://link.aps.org/doi/10.1103/PhysRevB.88.121102>.
- [16] Jiang, J. *et al.* Observation of possible topological in-gap surface states in the Kondo insulator SmB_6 by photoemission. Nat. Commun. **4** (2013). URL <http://dx.doi.org/10.1038/ncomms4010>.
- [17] Hundley, M. F., Canfield, P. C., Thompson, J. D., Fisk, Z. & Lawrence, J. M. Hybridization gap in $\text{Ce}_3\text{Bi}_4\text{Pt}_3$. Phys. Rev. B **42**, 6842–6845 (1990). URL <http://link.aps.org/doi/10.1103/PhysRevB.42.6842>.
- [18] Cooley, J. C., Aronson, M. C. & Canfield, P. C. High pressures and the Kondo gap in $\text{Ce}_3\text{Bi}_4\text{Pt}_3$. Phys. Rev. B **55**, 7533–7538 (1997). URL <http://link.aps.org/doi/10.1103/PhysRevB.55.7533>.
- [19] Hiess, A. *et al.* Transport properties of CeNiSn at low temperatures and in high magnetic fields. Physica B: Condensed Matter **199**, 437 – 439 (1994). URL <http://www.sciencedirect.com/science/article/pii/0921452694918627>.
- [20] Sera, M. *et al.* Anisotropic pseudogap in CeNiSn and CeRhSb studied by a thermal-conductivity measurement. Phys. Rev. B **55**, 6421–6428 (1997). URL <http://link.aps.org/doi/10.1103/PhysRevB.55.6421>.

- [21] Kawasaki, Y. et al. Energy gap formation in the valence fluctuating compound CeIrSb probed by Sb NMR and NQR. *Phys. Rev. B* **75**, 094410 (2007). URL <http://link.aps.org/doi/10.1103/PhysRevB.75.094410>.
- [22] Ślebarski, A. & Spalek, J. From Kondo semimetal to spin-glass behaviour in doped CeNi_{1-δ}Sn_{1+δ-x}Sb_x. *Philosophical Magazine* **89**, 1845–1859 (2009). URL <http://dx.doi.org/10.1080/14786430802647073>.
- [23] Shiozaki, K., Sato, M. & Gomi, K. Topology of nonsymmorphic crystalline insulators and superconductors. *ArXiv e-prints* (2015). 1511.01463.
- [24] Wang, Z., Alexandradinata, A., Cava, R. J. & Bernevig, B. A. Hourglass Fermions. *ArXiv e-prints* (2016). 1602.05585.
- [25] Lu, L. et al. Symmetry-protected topological photonic crystal in three dimensions. *Nat Phys* **12**, 337–340 (2016). URL <http://dx.doi.org/10.1038/nphys3611>.
- [26] Fang, C. & Fu, L. New classes of three-dimensional topological crystalline insulators: Nonsymmorphic and magnetic. *Phys. Rev. B* **91**, 161105 (2015). URL <http://link.aps.org/doi/10.1103/PhysRevB.91.161105>.
- [27] Shiozaki, K., Sato, M. & Gomi, K. Z_2 topology in nonsymmorphic crystalline insulators: Möbius twist in surface states. *Phys. Rev. B* **91**, 155120 (2015). URL <http://link.aps.org/doi/10.1103/PhysRevB.91.155120>.
- [28] Alexandrov, V., Coleman, P. & Erten, O. Kondo Breakdown in Topological Kondo Insulators. *Phys. Rev. Lett.* **114**, 177202 (2015). URL <http://link.aps.org/doi/10.1103/PhysRevLett.114.177202>.
- [29] Yanase, A. & Harima, H. Band Calculations on YbB₁₂, SmB₆ and CeNiSn **108**, 19–25 (1992). URL <http://ptps.oxfordjournals.org/content/108/19.abstract>.
- [30] Hammond, T. J., Gehring, G. A., Suvasini, M. B. & Temmerman, W. M. Electronic structures of CeNiSn, CePdSn, and CePtSn. *Phys. Rev. B* **51**, 2994–3002 (1995). URL <http://link.aps.org/doi/10.1103/PhysRevB.51.2994>.
- [31] Hiess, A. et al. Polarized neutron studies of CeNiSn. *Journal of Physics: Condensed Matter* **9**, 9321 (1997). URL <http://stacks.iop.org/0953-8984/9/i=43/a=016>.
- [32] Terashima, T. et al. Resistivity, Hall effect, and Shubnikov de Haas oscillations in CeNiSn. *Phys. Rev. B* **66**, 075127 (2002). URL <http://link.aps.org/doi/10.1103/PhysRevB.66.075127>.

- [33] Stockert, U. *et al.* Giant isotropic Nernst effect in an anisotropic Kondo semimetal. *ArXiv e-prints* (2016). 1603.01258.
- [34] Ekino, T., Takabatake, T., Tanaka, H. & Fujii, H. Tunneling Evidence for the Quasiparticle Gap in Kondo Semiconductors CeNiSn and CeRhSb. *Phys. Rev. Lett.* **75**, 4262–4265 (1995). URL <http://link.aps.org/doi/10.1103/PhysRevLett.75.4262>.
- [35] Nakamura, K.-i. *et al.* Impurity and doping effects on the pseudoenergy gap in CeNiSn: A Sn NMR study. *Phys. Rev. B* **53**, 6385–6392 (1996). URL <http://link.aps.org/doi/10.1103/PhysRevB.53.6385>.
- [36] Nakamura, K. *et al.* Low-Energy Excitation in Kondo Semiconductors CeNiSn and CeRhSb. *J. Phys. Soc. Jpn.* **63**, 433–436 (1994). URL <http://dx.doi.org/10.1143/JPSJ.63.433>.
- [37] Syers, P., Kim, D., Fuhrer, M. S. & Paglione, J. Tuning Bulk and Surface Conduction in the Proposed Topological Kondo Insulator SmB₆. *Phys. Rev. Lett.* **114**, 096601 (2015). URL <http://link.aps.org/doi/10.1103/PhysRevLett.114.096601>.
- [38] Nakajima, Y., Syers, P., Wang, X., Wang, R. & Paglione, J. One-dimensional edge state transport in a topological Kondo insulator. *Nat. Phys.* **advance online publication**, – (2015). URL <http://dx.doi.org/10.1038/nphys3555>.
- [39] Bennemann, K.-H. & Ketterson, J. B. *Superconductivity* (Springer, 2008). URL <http://www.springer.com/gp/book/9783540732525?token=prtst0416p>.
- [40] Huy, N. T. *et al.* Superconductivity on the Border of Weak Itinerant Ferromagnetism in UCoGe. *Phys. Rev. Lett.* **99**, 067006 (2007). URL <http://link.aps.org/doi/10.1103/PhysRevLett.99.067006>.
- [41] Aoki, D. *et al.* Coexistence of superconductivity and ferromagnetism in URhGe. *Nature* **413**, 613–616 (2001). URL <http://dx.doi.org/10.1038/35098048>.

VIII. MÖBIUS KONDO INSULATORS: SUPPLEMENTARY MATERIAL

A. A tight-binding model based on nonsymmorphic symmetries

Here we derive the tight-binding Hamiltonian for CeNiSn using the following procedure:

1. We define the symmetry operations on the fermionic operators.
2. We then construct the Hamiltonian by writing down the all the nearest neighbor hopping and hybridization terms which respect the nonsymmorphic symmetries.

In order to simplify our calculation, we introduce four sets of Pauli matrices: $\{\sigma_i\}$ acts on the spin basis; $\{\lambda_i\}$ acts on the basis of conduction electrons and f -electrons; $\{\tau_i\}$ acts on the basis of the atom labels 1 and 2; $\{\rho_i\}$ acts on the basis of the layer labels A and B .

In CeNiSn, $4f$ -electrons of Ce atoms hybridize with $3d$ -electrons of Ni atoms. Since the total angular momentum difference between these two states is one, we orbitally “downfold” the tight-binding model, replacing it by an equivalent model, reducing the total angular momentum J of each band by two units. The resulting model involves the hybridization of spin-orbit coupled p -electrons with s -electrons. The highly localized states are then modelled as p -wave Kramers doublets,

$$\begin{aligned} f_{\uparrow}^{\dagger}|0\rangle &\equiv |p_{x\downarrow} + ip_{y\downarrow} + p_{z\uparrow}\rangle \\ f_{\downarrow}^{\dagger}|0\rangle &\equiv |p_{x\uparrow} - ip_{y\uparrow} - p_{z\downarrow}\rangle. \end{aligned} \quad (5)$$

while the mobile conduction electrons are s -wave,

$$c_{\uparrow/\downarrow}^{\dagger}|0\rangle \equiv |s_{\uparrow/\downarrow}\rangle. \quad (6)$$

For further simplicity, we project the conduction electron Wannier states onto the sites of f -electrons.

B. Symmetries:

Here, we describe the actions of the various symmetry operations in space group No. 62 ($Pnma$) on the Fermi operators. This group contains three screw rotations $S_{x,y,z}$, three glide reflections $G_{x,y,z}$ and an inversion P . In fact, this set of six operators can all be generated from $G_z S_y$, in combination with inversion and translation operators, so it is sufficient for us to focus on these two non-symmorphic operators.

1. *Glide reflection* $G_z : (X, Y, Z) \rightarrow (X + 1/2, Y, -Z + 1/2)$

The glide reflection G_z transforms the f -electrons and conduction electrons as follows

$$\begin{aligned} G_z^{-1} f_{1L\sigma}^\dagger(\mathbf{x}_j) G_z &= -(i\sigma_3)_{\sigma\sigma'} f_{2L\sigma'}^\dagger(\mathbf{x}_j + c), \\ G_z^{-1} f_{2L\sigma}^\dagger(\mathbf{x}_j) G_z &= -(i\sigma_3)_{\sigma\sigma'} f_{1L\sigma'}^\dagger(\mathbf{x}_j + a + c), \end{aligned} \quad (7)$$

where \vec{x}_j is the co-ordinate of the unit cell, ($L \in [A, B]$) and 1 and 2 are the site and layer indices of atoms within one unit cell, a and c are unit vectors in the x and z directions, respectively, while σ is the spin index. The glide reflection acts in a similar way on the conduction electrons

$$\begin{aligned} G_z^{-1} c_{1L\sigma}^\dagger(\mathbf{x}_j) G_z &= (i\sigma_3)_{\sigma\sigma'} c_{2L\sigma'}^\dagger(\mathbf{x}_j + c), \\ G_z^{-1} c_{2L\sigma}^\dagger(\vec{x}_j) G_z &= (i\sigma_3)_{\sigma\sigma'} c_{1L\sigma'}^\dagger(\mathbf{x}_j + a + c). \end{aligned} \quad (8)$$

2. *Screw rotation* $S_y : (X, Y, Z) \rightarrow (-X, Y + 1/2, -Z)$

The screw rotation S_y transforms the f -electrons and conduction electrons as follows:

$$\begin{aligned} S_y^{-1} f_{1(2)A\sigma}^\dagger(\mathbf{x}_j) S_y &= i[\sigma_2]_{\sigma\sigma'} f_{1(2)B\sigma'}^\dagger(\mathbf{x}_j), \\ S_y^{-1} f_{1(2)B\sigma}^\dagger(\mathbf{x}_j) S_y &= i[\sigma_2]_{\sigma\sigma'} f_{1(2)A\sigma'}^\dagger(\mathbf{x}_j + b), \end{aligned} \quad (9)$$

and

$$\begin{aligned} S_y^{-1} c_{1(2)A\sigma}^\dagger(\mathbf{x}_j) S_y &= i[\sigma_2]_{\sigma\sigma'} c_{1(2)B\sigma'}^\dagger(\mathbf{x}_j), \\ S_y^{-1} c_{1(2)B\sigma}^\dagger(\mathbf{x}_j) S_y &= i[\sigma_2]_{\sigma\sigma'} c_{1(2)A\sigma'}^\dagger(\mathbf{x}_j + b), \end{aligned} \quad (10)$$

where b is the unit vector in y direction.

3. *Inversion* $P : (X, Y, Z) \rightarrow (-X, -Y, -Z)$

The inversion P transforms the f -electrons and conduction electrons in the following way,

$$\begin{aligned} P^{-1} f_{1(2)A\sigma}^\dagger(\mathbf{x}_j) P &= -f_{1(2)B\sigma}^\dagger(\mathbf{x}_j), \\ P^{-1} f_{1(2)B\sigma}^\dagger(\mathbf{x}_j) P &= -f_{1(2)A\sigma}^\dagger(\mathbf{x}_j). \end{aligned} \quad (11)$$

And

$$\begin{aligned} P^{-1} c_{1(2)A\sigma}^\dagger(\mathbf{x}_j) P &= c_{1(2)B\sigma}^\dagger(\mathbf{x}_j), \\ P^{-1} c_{1(2)B\sigma}^\dagger(\mathbf{x}_j) P &= c_{1(2)A\sigma}^\dagger(\mathbf{x}_j). \end{aligned} \quad (12)$$

4. Other symmetries:

By combining inversion, translations, and the above two nonsymmorphic symmetries we can obtain all the remaining symmetries. Thus $G_x = T_{(1,0,1)}S_yG_z$, and $G_y : (X, Y, Z) \rightarrow (X, -Y + 1/2, Z)$, since

$$(X, Y, Z) \xrightarrow{G_z} (X + 1/2, Y, -Z + 1/2) \xrightarrow{S_y} (-X - 1/2, Y + 1/2, Z - 1/2) \xrightarrow{T_{(1,0,1)}} (-X + 1/2, Y + 1/2, Z + 1/2), \quad (13)$$

and likewise,

$$(X, Y, Z) \xrightarrow{S_y} (-X, Y + 1/2, -Z) \xrightarrow{P} (X, -Y - 1/2, Z) \xrightarrow{T_{(0,1,0)}} (X, -Y + 1/2, Z). \quad (14)$$

In a similar fashion, we obtain $S_x = T_{(1,1,1)}PG_x$ and $S_z = T_{(1,0,1)}PG_z$, since

$$(X, Y, Z) \xrightarrow{G_x} (-X + 1/2, Y + 1/2, Z + 1/2) \xrightarrow{P} (X - 1/2, -Y - 1/2, -Z - 1/2) \xrightarrow{T_{(1,1,1)}} (X + 1/2, -Y + 1/2, Z + 1/2). \quad (15)$$

and

$$(X, Y, Z) \xrightarrow{G_z} (X + 1/2, Y, -Z + 1/2) \xrightarrow{P} (-X - 1/2, -Y, Z - 1/2) \xrightarrow{T_{(1,0,1)}} (-X + 1/2, -Y, Z + 1/2). \quad (16)$$

C. Construction of the Hamiltonian

1. Hopping terms

Now we consider the nearest neighbor hopping terms in the Hamiltonian [see Fig. 5].

$$\begin{aligned} H^{\text{hopping}} = & \sum_{j,\sigma,l=c,f} t_x^l l_{1A\sigma}^\dagger(\mathbf{x}_j) l_{2A\sigma}(\mathbf{x}_j) + t_x^l l_{2A\sigma}^\dagger(\mathbf{x}_j) l_{1A\sigma}(\mathbf{x}_j + a) + t_z^l l_{1A\sigma}^\dagger(\mathbf{x}_j) l_{1A\sigma}(\mathbf{x}_j + c) \\ & + t_z^l l_{1B\sigma}^\dagger(\mathbf{x}_j) l_{1B\sigma}(\mathbf{x}_j + c) + t_y^l l_{1A\sigma}^\dagger(\mathbf{x}_j) l_{2B\sigma}(\mathbf{x}_j) + t_y^l l_{2A\sigma}^\dagger(\mathbf{x}_j) l_{1B\sigma}(\mathbf{x}_j) \\ & + t_y^l l_{1B\sigma}^\dagger(\mathbf{x}_j) l_{2A\sigma}(\mathbf{x}_j + b) + t_y^l l_{2B\sigma}^\dagger(\mathbf{x}_j) l_{1A\sigma}(\mathbf{x}_j + b) \\ & - \sum_{\alpha=1,2;L=A,B;j;\sigma;l=c,f} \mu^l l_{\alpha L\sigma}^\dagger(\mathbf{x}_j) l_{\alpha L\sigma}(\mathbf{x}_j) + \text{h.c.}, \end{aligned} \quad (17)$$

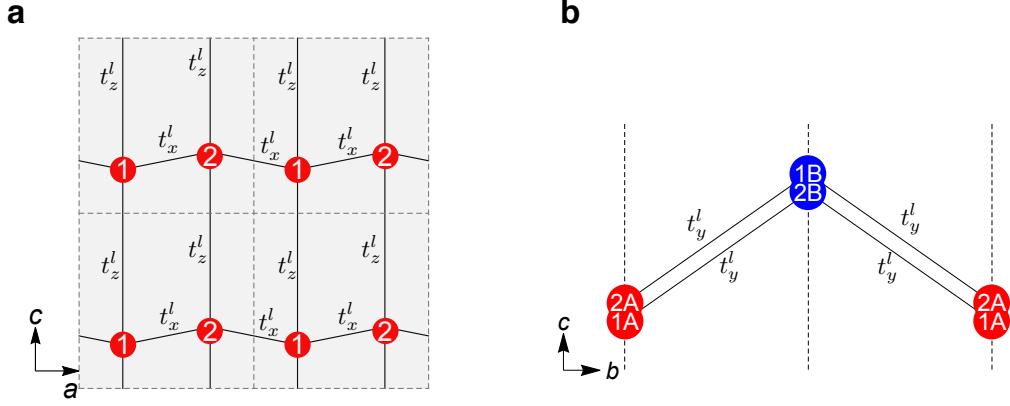


FIG. 5. **Hopping Hamiltonian:** **a**, The hopping elements t_x^l and t_z^l with $l = c, f$ on the ac plane. **b**, The hopping elements t_y^l with $l = c, f$ on the bc plane.

where t_i^l is the hopping amplitude for $l = c, f$ electrons along i direction, and μ^l is the on-site chemical potential for $l = c, f$ electrons. The hopping Hamiltonian is explicitly invariant under G_z , S_y and P , and since all the other non-symmorphic symmetries can be expanded in terms of these three (plus translation), the hopping is invariant under the full non-symmorphic group.

In momentum space, the hopping Hamiltonian is $H^{\text{hopping}} = \sum_{\mathbf{k}} \Psi(\mathbf{k})^\dagger \mathcal{H}^{\text{hopping}}(\mathbf{k}) \Psi(\mathbf{k})$, where where $\Psi^\dagger(\mathbf{k})$ is a sixteen component creation operator, $\Psi^\dagger(\mathbf{k}) = (\Psi_c^\dagger(\mathbf{k}), \Psi_f^\dagger(\mathbf{k}))$ with

$$\begin{aligned} \Psi_c^\dagger(\mathbf{k}) &= (c_{1A\uparrow}^\dagger(\mathbf{k}), c_{1A\downarrow}^\dagger(\mathbf{k}), c_{2A\uparrow}^\dagger(\mathbf{k}), c_{2A\downarrow}^\dagger(\mathbf{k}), c_{1B\uparrow}^\dagger(\mathbf{k}), c_{1B\downarrow}^\dagger(\mathbf{k}), c_{2B\uparrow}^\dagger(\mathbf{k}), c_{2B\downarrow}^\dagger(\mathbf{k})), \\ \Psi_f^\dagger(\mathbf{k}) &= (f_{1A\uparrow}^\dagger(\mathbf{k}), f_{1A\downarrow}^\dagger(\mathbf{k}), f_{2A\uparrow}^\dagger(\mathbf{k}), f_{2A\downarrow}^\dagger(\mathbf{k}), f_{1B\uparrow}^\dagger(\mathbf{k}), f_{1B\downarrow}^\dagger(\mathbf{k}), f_{2B\uparrow}^\dagger(\mathbf{k}), f_{2B\downarrow}^\dagger(\mathbf{k})), \end{aligned}$$

and

$$\mathcal{H}^{\text{hopping}}(\mathbf{k}) = \begin{pmatrix} \mathcal{H}^c(\mathbf{k}) & 0 \\ 0 & \mathcal{H}^f(\mathbf{k}) \end{pmatrix}, \quad (18)$$

with

$$\begin{aligned} \mathcal{H}^{c/f}(\mathbf{k}) &= (2t_z^{c/f} \cos k_z - \mu^{c/f}) + 2t_x^{c/f} \cos \frac{k_x}{2} \left(\cos \frac{k_x}{2} \tau_1 + \sin \frac{k_x}{2} \tau_2 \rho_3 \right) \\ &\quad + 2t_y^{c/f} \cos \frac{k_y}{2} \left(\cos \frac{k_y}{2} \tau_1 \rho_1 + \sin \frac{k_y}{2} \tau_1 \rho_2 \right). \end{aligned} \quad (19)$$

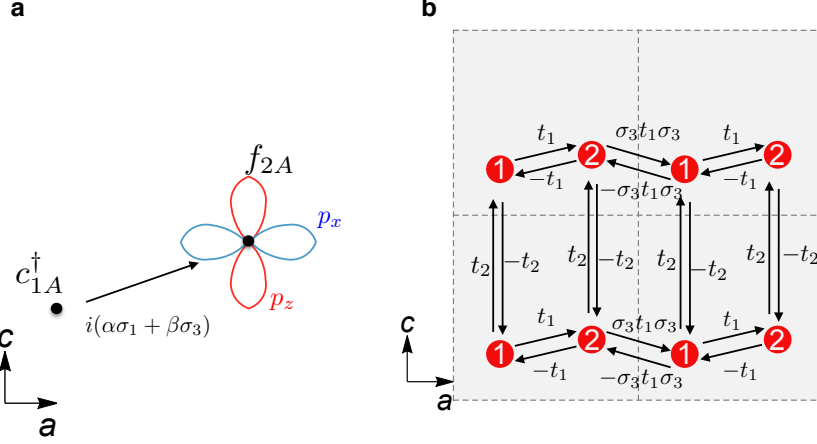


FIG. 6. **Hybridization Hamiltonian on A layer:** **a**, The hybridization matrix between c_{1A}^\dagger and f_{2A} is $t_1 = i(\alpha\sigma_1 + \beta\sigma_3)$. **b**, The hybridization elements t_1 , $\sigma_3 t_1 \sigma_3$ and t_2 on the ac plane.

2. Hybridization terms

We now consider the hybridization terms between f -electrons and conduction electrons. Let us start with layer A . The hybridization Hamiltonian on layer A is (see Fig. 6b)

$$\begin{aligned}
 H_A^{\text{hybr.}} = & \sum_{j,\sigma,\sigma'} c_{1A\sigma}^\dagger(\mathbf{x}_j)[t_1]_{\sigma\sigma'} f_{2A\sigma'}(\mathbf{x}_j) - c_{2A\sigma}^\dagger(\mathbf{x}_j)[t_1]_{\sigma\sigma'} f_{1A\sigma'}(\mathbf{x}_j) + c_{1A\sigma}^\dagger(\mathbf{x}_j)[t_2]_{\sigma\sigma'} f_{1A\sigma'}(\mathbf{x}_j + c) \\
 & + c_{2A\sigma}^\dagger(\mathbf{x}_j)[t_2]_{\sigma\sigma'} f_{2A\sigma'}(\mathbf{x}_j + c) + G_z^{-1}(\dots)G_z + \text{h.c.}, \quad (20)
 \end{aligned}$$

where $G_z^{-1}(\dots)G_z$ in the second line is the glide-reflection of the first four terms. This guarantees that $G_z^{-1}H_A^{\text{hybr.}}G_z = H_A^{\text{hybr.}}$. The hybridization matrices have the structure $t_1 = i(\alpha\sigma_1 + \beta\sigma_3)$, and $t_2 = i\gamma\sigma_3$ (see Fig. 6a). In momentum space, the hybridization Hamiltonian on layer A is $H_A^{\text{hybr.}} = \sum_{\mathbf{k}} \Psi_A^\dagger(\mathbf{k})\mathcal{H}_A^{\text{hybr.}}(\mathbf{k})\Psi_A(\mathbf{k})$, where

$$\Psi_A^\dagger(\mathbf{k}) = (c_{1A\uparrow}^\dagger(\mathbf{k}), c_{1A\downarrow}^\dagger(\mathbf{k}), c_{2A\uparrow}^\dagger(\mathbf{k}), c_{2A\downarrow}^\dagger(\mathbf{k}), f_{1A\uparrow}^\dagger(\mathbf{k}), f_{1A\downarrow}^\dagger(\mathbf{k}), f_{2A\uparrow}^\dagger(\mathbf{k}), f_{2A\downarrow}^\dagger(\mathbf{k})) \quad (21)$$

and

$$\mathcal{H}_A^{\text{hybr.}}(\mathbf{k}) = \begin{pmatrix} 0 & V_A(\mathbf{k}) \\ V_A(\mathbf{k})^\dagger & 0 \end{pmatrix}, \quad \text{with} \quad V_A(\mathbf{k}) = \begin{pmatrix} 2it_2 \sin k_z & t_1 + \sigma_3 t_1 \sigma_3 e^{-ik_x} \\ -t_1 - \sigma_3 t_1 \sigma_3 e^{ik_x} & 2it_2 \sin k_z \end{pmatrix}. \quad (22)$$

The hybridization Hamiltonian on the B layer can be obtained by performing the screw rotation S_y on $H_A^{\text{hybr.}}$, $H_B^{\text{hybr.}} = S_y^{-1}H_A^{\text{hybr.}}S_y$.

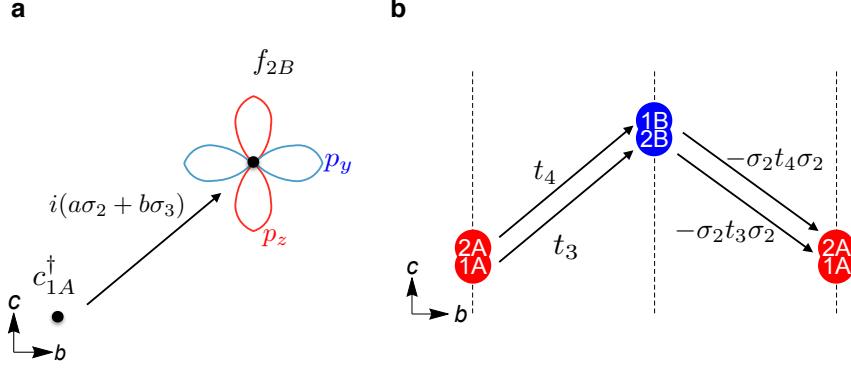


FIG. 7. **Interlayer hybridization Hamiltonian:** **a**, The interlayer hybridization matrix between c_{1A}^\dagger and f_{2A} is $t_3 = i(a\sigma_2 + b\sigma_3)$. **b**, The interlayer hybridization elements t_3 and t_4 on the bc plane.

Next, we write down the interlayer hybridization terms. The interlayer hybridization Hamiltonian (see Fig. 7b) is

$$\begin{aligned}
H_{AB}^{\text{hybr.}} = & \sum_{j,\sigma,\sigma'} c_{1A\sigma}^\dagger(\mathbf{x}_j)[t_3]_{\sigma\sigma'} f_{2B\sigma'}(\mathbf{x}_j) + c_{2A\sigma}^\dagger(\mathbf{x}_j)[t_4]_{\sigma\sigma'} f_{1B\sigma'}(\mathbf{x}_j) + \\
& + S_y^{-1}(\dots)S_y + P^{-1}(\dots)P + [PS_y]^{-1}(\dots)PS_y + \text{h.c.}, \quad (23)
\end{aligned}$$

where (\dots) denote a repeat of the first two terms, $t_3 = i(a\sigma_2 + b\sigma_3)$ and $t_4 = i(a\sigma_2 - b\sigma_3)$ (see Fig. 7a). By construction, interlayer hybridization is invariant under G_z , S_y and P , and is thus invariant under the full non-symmorphic group. In momentum space, the interlayer hybridization Hamiltonian is $H_{AB}^{\text{hybr.}} = \sum_{\mathbf{k}} \Psi(\mathbf{k})^\dagger \mathcal{H}_{AB}^{\text{hybr.}}(\mathbf{k}) \Psi(\mathbf{k})$, where

$$\begin{aligned}
\mathcal{H}_{AB}^{\text{hybr.}}(\mathbf{k}) = & \begin{pmatrix} & & & V_{AB}(\mathbf{k}) \\ & & & \\ & & V_{BA}(\mathbf{k})^\dagger & \\ & & & \\ & & V_{BA}(\mathbf{k}) & \\ & & & \\ V_{AB}(\mathbf{k})^\dagger & & & \end{pmatrix}, \quad \text{with} \\
V_{AB}(\mathbf{k}) = & \begin{pmatrix} & t_3 - \sigma_2 t_3 \sigma_2 e^{-ik_y} \\ t_4 - \sigma_2 t_4 \sigma_2 e^{-ik_y} & \end{pmatrix}, \quad V_{BA}(\mathbf{k}) = \begin{pmatrix} & \sigma_2 t_3 \sigma_2 e^{ik_y} - t_3 \\ \sigma_2 t_4 \sigma_2 e^{ik_y} - t_4 & \end{pmatrix}. \quad (24)
\end{aligned}$$

3. Full Hamiltonian

Finally, we obtain the total single-particle Hamiltonian

$$\mathcal{H}(\mathbf{k}) = \begin{pmatrix} \mathcal{H}^c(\mathbf{k}) & V(\mathbf{k}) \\ V^\dagger(\mathbf{k}) & \mathcal{H}^f(\mathbf{k}) \end{pmatrix}, \quad (25)$$

where $\mathcal{H}^{c/f}(\mathbf{k})$ is defined in equation (19), and

$$V(\mathbf{k}) = \begin{pmatrix} V_A(\mathbf{k}) & V_{AB}(\mathbf{k}) \\ V_{BA}(\mathbf{k}) & V_B(\mathbf{k}) \end{pmatrix},$$

with $V_A(\mathbf{k})$ being defined in equation (22) and $V_{AB}(\mathbf{k})$, $V_{BA}(\mathbf{k})$ being defined in equation (24).

4. Matrix representation of symmetries

Once we fix the basis of the spinor $\Psi(\mathbf{k})$, we can write down all matrix representations of symmetries in momentum space. The glide reflection is

$$\mathcal{G}_z(\mathbf{k}) = -ie^{-i\frac{k_x}{2}} \sigma_3 \left(\cos \frac{k_x}{2} \tau_1 + \sin \frac{k_x}{2} \tau_2 \rho_3 \right) \lambda_3, \quad (26)$$

while the screw rotation and inversion symmetry in the momentum space are

$$\begin{aligned} \mathcal{S}_y(\mathbf{k}) &= -ie^{-i\frac{k_y}{2}} \sigma_2 \tau_0 \lambda_0 \left(\cos \frac{k_y}{2} \rho_1 + \sin \frac{k_y}{2} \rho_2 \right), \\ \mathcal{P} &= \sigma_0 \tau_0 \lambda_3 \rho_1. \end{aligned} \quad (27)$$

It can be verified that $\mathcal{G}_z(\mathbf{k})^{-1} \mathcal{H}(k_x, k_y, k_z) \mathcal{G}_z(\mathbf{k}) = \mathcal{H}(k_x, k_y, -k_z)$, and that $\mathcal{G}_z(\mathbf{k})^2 = -e^{-ik_x}$, as expected from the combination of full translation and twice reflections (see equation (1) in main text). Similarly, one can verify that the Hamiltonian transforms under \mathcal{S}_y as $\mathcal{S}_y(\mathbf{k})^{-1} \mathcal{H}(k_x, k_y, k_z) \mathcal{S}_y(\mathbf{k}) = \mathcal{H}(-k_x, k_y, -k_z)$ and under inversion, $\mathcal{P}^{-1} \mathcal{H}(\mathbf{k}) \mathcal{P} = \mathcal{H}(-\mathbf{k})$. In a similar fashion to the glide reflection, $\mathcal{S}_y(\mathbf{k})^2 = -e^{-ik_y}$, which is expected from a 2π rotation and one full lattice translation. The transformation of the Hamiltonian under the full set of non-symmorphic symmetries can be obtained by decomposing them in terms of \mathcal{G}_z and \mathcal{S}_y , as described in (VIII B 4).

Time-reversal symmetry has the usual representation, $\mathcal{T} = i\sigma_2 \mathcal{K}$, where \mathcal{K} is the complex conjugation operator. We have $\mathcal{T}^{-1} \mathcal{H}(\mathbf{k}) \mathcal{T} = \mathcal{H}(-\mathbf{k})$.

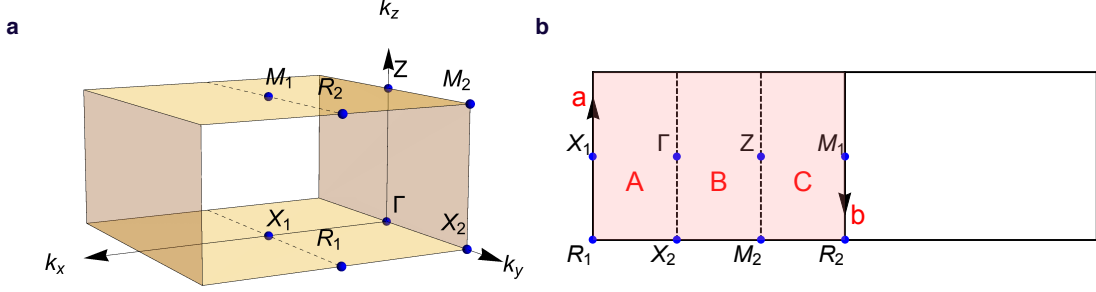


FIG. 8. **Illustration of calculating the \mathbb{Z}_4 invariant.** **a**, The "bent" BZ (shaded in yellow) is chosen by connecting two glide planes to their neighboring plane, which is traversing half the BZ at $k_x = 0$. **b**, The \mathbb{Z}_4 invariant in equation (29) is calculated in the half of the "bent" BZ (shaded in red).

D. \mathbb{Z}_4 topological invariant

We give the definition of the \mathbb{Z}_4 invariant in symmetry class AII introduced in Ref. [1]. In the presence of the glide reflection symmetry \mathcal{G}_z , there are two glide planes in the BZ at $k_z = 0$ and $k_z = \pi$. In these glide planes, the occupied states can be separated into two sectors with the glide eigenvalues $g_{\pm} = \pm i e^{-ik_x/2}$. Due to the bulk-boundary correspondence, the existence of protected surface modes on glide planes are associated with the Berry connections and Berry curvature on the "bent" BZ [2]. This "bent" BZ is chosen by connecting two glide planes to their neighboring plane, which is traversing half the BZ at $k_x = 0$ (Fig. 8a). In the main text, we demonstrate the number of Dirac cones along path $X'\Gamma XMZM'X'$ is modulo four, which implies that the \mathbb{Z}_4 invariant can be defined from calculating the winding number of the Berry connections of two glide sectors on the "bent" BZ. Having the same spirit of calculating the \mathbb{Z}_2 invariant in time-reversal symmetric system, we only need to consider the half of the "bent" BZ as shown in Fig. 8b. Along paths a and b , the eigenvalues of glide reflection symmetry are real and the Kramers pairs ($|u_{\mu}^{\pm,I}(\mathbf{k})\rangle, |u_{\mu}^{\pm,II}(\mathbf{k})\rangle$) are in the same glide sector. We have

$$\oint_{a(b)} dl \mathcal{A}^{\pm} = 2 \oint_{a(b)} dl \mathcal{A}^{\pm,I} \pmod{2\pi}, \quad (28)$$

where $\mathcal{A}^{\pm,I} = i \sum_{\mu \in \text{occ.}} \langle u_{\mu}^{\pm,I}(\mathbf{k}) | \partial_{k_y} u_{\mu}^{\pm,I}(\mathbf{k}) \rangle$, and $\mathcal{A}^{\pm} = i \sum_{\mu \in \text{occ.}} \langle u_{\mu}^{\pm,I}(\mathbf{k}) | \partial_{k_y} u_{\mu}^{\pm,I}(\mathbf{k}) \rangle + \langle u_{\mu}^{\pm,II}(\mathbf{k}) | \partial_{k_y} u_{\mu}^{\pm,II}(\mathbf{k}) \rangle$.

The \mathbb{Z}_4 invariant is defined by consider the positive glide sector at glide plane. We have

$$\chi := \frac{1}{2\pi} [4 \oint_a dl \mathcal{A}^{+,I} - 4 \oint_b dl \mathcal{A}^{+,I} - (2 \int_A da \mathcal{F}^+ + 2 \int_C da \mathcal{F}^+ + \int_B da \mathcal{F})], \pmod{4}, \quad (29)$$

where the Berry curvature is defined as $\mathcal{F}^\pm = \partial_t \mathcal{A}^\pm - \partial_{k_y} \mathcal{A}^\pm$ with t being the momentum direction which perpendicular to k_y on the "bent BZ" and $\mathcal{F} = \mathcal{F}^+ + \mathcal{F}^-$.

E. Resistivity plateau in doped $\text{CeNi}_{1-\delta}\text{Sn}_{1+\delta-x}\text{Sb}_x$ and $\text{Ce}_3\text{Bi}_4\text{Pt}_3$

Fig 9 shows the resistivity plateau at low temperature of doped $\text{CeNi}_{1-\delta}\text{Sn}_{1+\delta-x}\text{Sb}_x$ and $\text{Ce}_3\text{Bi}_4\text{Pt}_3$ under pressure.

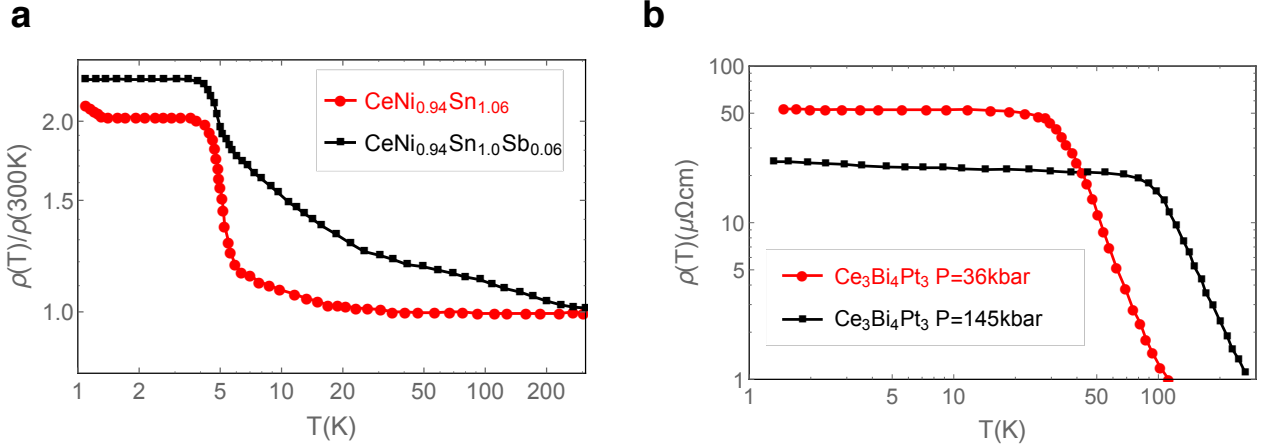


FIG. 9. Resistivity versus temperature adapted from Refs. [3 and 4]: a, doped $\text{CeNi}_{1-\delta}\text{Sn}_{1+\delta-x}\text{Sb}_x$. b, $\text{Ce}_3\text{Bi}_4\text{Pt}_3$ under pressure.

-
- [1] Shiozaki, K., Sato, M. & Gomi, K. Topology of nonsymmorphic crystalline insulators and superconductors. *ArXiv e-prints* 1511.01463.
- [2] Alexandradinata, A., Fang, C., Gilbert, M. J. & Bernevig, B. A. Spin-orbit-free topological insulators without time-reversal symmetry. *Phys. Rev. Lett.* **113**, 116403 (2014). URL <http://link.aps.org/doi/10.1103/PhysRevLett.113.116403>.
- [3] Ślebarski, A. & Spalek, J. From Kondo semimetal to spin-glass behaviour in doped $\text{CeNi}_{1-\delta}\text{Sn}_{1+\delta-x}\text{Sb}_x$ system. *Philosophical Magazine* **89**, 1845–1859 (2009). URL <http://dx.doi.org/10.1080/14786430802647073>.
- [4] Cooley, J. C., Aronson, M. C. & Canfield, P. C. High pressures and the Kondo gap in $\text{Ce}_3\text{Bi}_4\text{Pt}_3$ s. *Phys. Rev. B* **55**, 7533–7538 (1997). URL <http://link.aps.org/doi/10.1103/PhysRevB.55.7533>.